

# Field Characterization and Compensation of Vibrational Nonuniformity for a 256-Element Focused Ultrasound Phased Array

Mohamed A. Ghanem<sup>1</sup>, Adam D. Maxwell<sup>2</sup>, Wayne Kreider, Bryan W. Cunitz, Vera A. Khokhlova<sup>3</sup>, Oleg A. Sapozhnikov, and Michael R. Bailey<sup>4</sup>

**Abstract**—Multielement focused ultrasound phased arrays have been used in therapeutic applications to treat large tissue volumes by electronic steering of the focus, to target multiple simultaneous foci, and to correct aberration caused by inhomogeneous tissue pathways. There is an increasing interest in using arrays to generate more complex beam shapes and corresponding acoustic radiation force patterns for manipulation of particles such as kidney stones. Toward this end, experimental and computational tools are needed to enable accurate delivery of desired transducer vibrations and corresponding ultrasound fields. The purpose of this paper was to characterize the vibrations of a 256-element array at 1.5 MHz, implement strategies to compensate for variability, and test the ability to generate specified vortex beams that are relevant to particle manipulation. The characterization of the array output was performed in water using both element-by-element measurements at the focus of the array and holography measurements for which all the elements were excited simultaneously. Both methods were used to quantify each element's output so that the power of each element could be equalized. Vortex beams generated using both compensation strategies were measured and compared to the Rayleigh integral simulations of fields generated by an idealized array based on the manufacturer's specifications. Although both approaches improved beam axisymmetry, compensation based on holography measurements had half the error relative to the simulation results in comparison to the element-by-element method.

**Index Terms**—Acoustic beam shaping, apodization, element-by-element (far field) measurements, holography, hydrophone angular response, radiation force balance (RFB).

Manuscript received February 8, 2018; accepted June 22, 2018. Date of publication June 27, 2018; date of current version August 29, 2018. This work was supported in part by the NSBRI under Grant NASA NCC 9-58, in part by the RSF under Grant 14-12-00974, in part by the NIH NIBIB under Grant RO1-EB007643, and in part by the NIDDK under Grant P01-DK043881, Grant NIH RO1-EB025187, and Grant K01-DK104854. (Corresponding author: Mohamed A. Ghanem.)

M. A. Ghanem is with the Department of Aeronautics and Astronautics Engineering, University of Washington, Seattle, WA 98195 USA, and also with the Applied Physics Laboratory, Center for Industrial and Medical Ultrasound, University of Washington, Seattle, WA 98105 USA (e-mail: mghanem@uw.edu).

A. D. Maxwell and M. R. Bailey are with the Applied Physics Laboratory, Center for Industrial and Medical Ultrasound, University of Washington, Seattle, WA 98105 USA, and also with the Department of Urology, University of Washington School of Medicine, Seattle, WA 98195 USA.

W. Kreider and B. W. Cunitz are with the Applied Physics Laboratory, Center for Industrial and Medical Ultrasound, University of Washington, Seattle, WA 98105 USA.

V. A. Khokhlova and O. A. Sapozhnikov are with the Physics Faculty, M. V. Lomonosov Moscow State University, 119991 Moscow, Russia, and also with the Applied Physics Laboratory, Center for Industrial and Medical Ultrasound, University of Washington, Seattle, WA 98105 USA.

Digital Object Identifier 10.1109/TUFFC.2018.2851188

## I. INTRODUCTION

MULTIELEMENT focused ultrasound phased arrays have been used in therapeutic applications to treat large volumes by electronic steering of the focus, to target multiple simultaneous foci, and to correct aberration caused by inhomogeneous tissue pathways. There is an increasing interest in using arrays to generate more complex beam shapes and corresponding acoustic radiation force patterns for noncontact manipulation of particles [1]–[3]. One emerging application for this effect is noninvasive repositioning of urinary stones to facilitate stone clearance [4]–[6]. Vortex beams are characterized by null pressure in the center and a toroidal-like acoustic beam shape [7]–[9]. Such beams offer the possibility of pulling [10]–[12], pushing [10], [13], or trapping an object [3], [14]. In the idealized case, a continuous axisymmetric transducer can generate a vortex beam if the phase varies linearly with the polar angle around the transducer's acoustic axis with a maximum phase delay of  $2\pi M$  radians. Here,  $M$  is an integer number known as the topological charge, which controls the wavefront helicity and the overall toroidal width.

In this effort, we seek to reproduce such beams using a phased array transducer. Although such an implementation involves inherent challenges related to finite-element sizes, phased arrays do provide the appealing potential to electronically steer beams and any trapped objects in 3-D space. To realize the generation of vortex beams with a phased array transducer, the first step is to characterize its output in order to account for nonuniform behavior of each element. Successful characterization and compensation of nonuniformity will provide a basis for the future efforts to synthesize specific beam shapes to trap and manipulate objects such as urinary stones by means of acoustic radiation force.

The simplest method to characterize a focused array involves element-by-element measurements for which the hydrophone is placed in the geometric focus of the array and each element is excited individually to measure the amplitude and the phase differences among the elements [15], [16]. Several studies have utilized this method to apply phase corrections to yield a high focal intensity in the presence of a scatterer [17]–[19] and to test focal steering capabilities [16], [20], [21]. Time reversal [22]–[24] is another method which uses the reflection of acoustic signals generated, and

often received, by each element from a focal target. It has been used to correct for phase aberration as well as nonuniform attenuation introduced by propagation through heterogeneous media [25], [26]. In the third method, element-by-element measurements were taken at multiple locations in the field. This has been used to determine array excitation vectors using a pseudoinverse method [17], to maximize focal intensity and to produce multiple foci [27]–[29]. In this paper, a method is developed to determine the required individual adjustments to the vibratory amplitude and phase of each element of the array as needed to generate accurate and uniform complex 2-D beam shapes.

Acoustic holography and element-by-element method are used here to quantify the complex output of every element. In acoustic holography, a 2-D scan of the field produced by excitation of the entire array is measured and used as a boundary condition to reconstruct the field at the transducer surface or anywhere in 3-D space [30], [31]. Holographic back-propagation of vortex beams was introduced in [7]. The evolution of an unfocused vortex beam along the propagation axis was examined. Holography captures effects caused by crosstalk and eliminates the variability between elements when driven sequentially due to the transient response of the power supply. It has been shown that power sources alone can introduce phase differences between elements that reduce focal intensities by 20%–30% [18], and such effects are missed with an element-by-element approach. Compared to holography, element-by-element methods have a limited ability to quantify the vibrations of each element. In particular, such approaches typically require an assumption that each element vibrates uniformly over some prescribed aperture. With this assumption, a pressure measurement at a single point in the far field can be readily related to the element's vibration magnitude. However, this approach cannot account for nonuniform vibrations within each element or effective element sizes that differ from assumed values. Because each element's effective aperture influences its directivity, the synthesis of complex 2-D fields will be hindered by such assumptions. Moreover, element-by-element approaches are inherently incapable of capturing the effects of crosstalk among elements and amplifier channels.

The purpose of this paper was to characterize a 1.5 MHz, 256-element transducer array, compensate for differences in the phase and the amplitude between the array elements, and demonstrate an improvement in the array performance in the generation of uniform vortex beams. First, the transducer was matched electrically to a Verasonics Data Acquisition system (VDAS) for efficient power transfer. Then, element-by-element and holography measurements were acquired to quantify each element's output. As a part of the holography approach, a method was developed to identify the performance characteristics of each element. Compensation strategies based on both measurement approaches were implemented to equalize the phase and the amplitude across all the elements. The performance of these compensation strategies was tested by evaluating the uniformity of vortex beams.

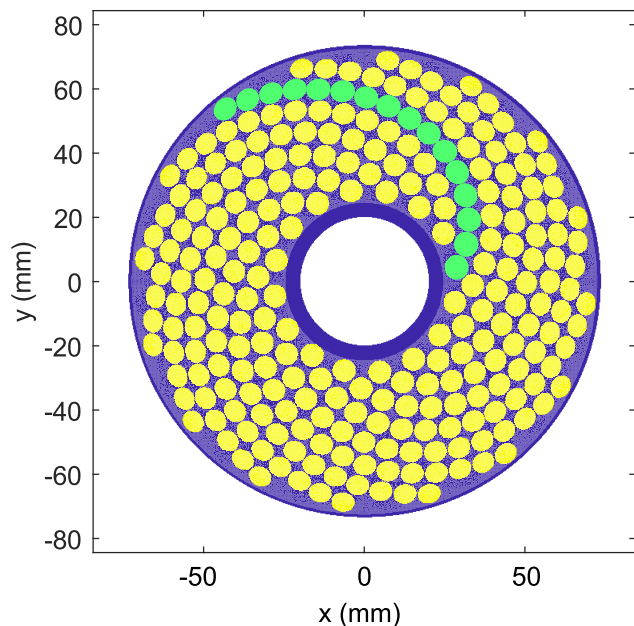


Fig. 1. Photograph of the array (top). 2-D layout of the array (bottom). The array has 16 spirals with 16 elements in each spiral for a total of 256 elements. Each element has a nominal diameter of 7 mm with interelement gaps of 0.5 mm. Central opening is 40 mm, and active acoustic aperture is 147 mm.

## II. METHODS

The transducer characterized in this paper is a piezocomposite array manufactured by Imasonic, SAS, Voray sur l'Ognon, France [32]. The array is geometrically focused with a spherical radius of curvature of 120 mm. The mechanical aperture is 160 mm; the active acoustic aperture is 147 mm, including a central opening of 40 mm in diameter (Fig. 1). The 256 piezocomposite elements are arranged in 16 spirals with each spiral having 16 elements. The diameter of each element is 7 mm with interelement gaps of 0.5 mm. The face of the transducer is acoustically matched to water at a nominal frequency of 1.5 MHz to yield a 1.2–1.8-MHz working

TABLE I  
AVERAGE IMPEDANCE (OHMS) OF ARRAY ELEMENTS  
BEFORE AND AFTER TUNING WITH INDUCTORS

Impedance	Re(Z) (Ohms)	Im(Z) (Ohms)
Untuned	$59.1 \pm 3.8$	$-207.9 \pm 3.2$
Tuned	$72.2 \pm 4.9$	$-13 \pm 6.6$

frequency range and a manufacturer-reported efficiency in excess of 63%.

#### A. Electrical Measurements

The transducer was driven electrically using a VDAS (V-1, Verasonics, LTD., Kirkland, WA, USA), a research ultrasound engine with a 1200-W external power source (QPX600DP, Aim-TTI, Huntingdon, U.K.). The array was electrically tuned using a series inductor for each element to eliminate the imaginary component of the impedance and thus to optimize the driving efficiency at 1.5 MHz. The inductors were mounted on the two printed circuit boards. The ferrite-core shielded inductors were used to reduce the electrical crosstalk between the channels. Crosstalk was measured by triggering a single element and monitoring the voltage output of an adjacent element on the circuit board. The maximum voltage on all the monitored adjacent elements was measured to be 0.08% of the voltage signal on the excited element on each circuit board, which was insignificant.

All elements were tuned with the same inductance. The impedance after matching was measured using an impedance analyzer (Antenna Analyzer AIM-4170D, Array solutions Sunnyvale, TX, USA) and compared with values before matching (Table I). Ideally, the inductors network should be lossless; however, an increase in the average real impedance of 22% was measured, which translated to 18% power losses in the inductors. However, a comparison before and after tuning shows that the electrical power delivered is 7 times the power delivered without the electrical tuning. A small nonzero imaginary component remained on most elements (Table I) as the inductors were chosen in discrete values only, and the inductances were measured to be slightly smaller than their nominal value at high frequencies. The total electrical power delivered to the transducer ( $W_{\text{tot}}$ ) was calculated using the following equation:

$$W_{\text{tot}} = \sum_{j=1}^{256} W_j = \sum_{j=1}^{256} \frac{|V_j|^2}{2} \text{Re} \left( \frac{1}{Z_j} \right) \quad (1)$$

where  $Z_j$  is the complex electrical impedance measured in ohms and  $V_j$  is the voltage on element  $j$  measured after matching. In Table I, the negative imaginary impedance indicates that the reactive component is capacitive.

#### B. Acoustical Measurements

A total of four experiments were performed in the study at the transducer operating frequency of 1.5 MHz:

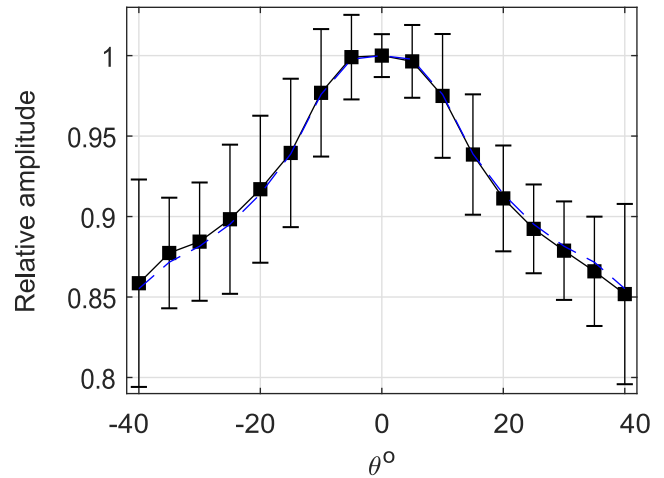


Fig. 2. Angular response up to  $40^\circ$  of the HGL-0200 Onda capsule hydrophone (sensing element diameter  $200 \mu\text{m}$ ). Black solid curve represents experimental data with error bars of eight angular sweeps; each sweep is performed twice along a different azimuthal angle. Blue dashed line represents the average of the left and right halves of the experimental data, based on a symmetric response assumption.

- 1) element-by-element measurements for acoustic characterization of the array and equalization of the element outputs;
- 2) holography measurements for a comparable acoustic characterization;
- 3) radiation force balance (RFB) measurements [33] to independently quantify the power output of the array;
- 4) the 2-D hydrophone scans to measure the uniformity of the vortex beam shapes before and after compensation.

All the experiments were performed in a tank of degassed and deionized water. Except for RFB experiments, all measurements utilized a capsule hydrophone (HGL-0200 with AH-2020 preamplifier, Onda Corporation, Sunnyvale, CA, USA). As per the manufacturer's calibration, the integrated hydrophone sensitivity at 1.5 MHz was  $416 \text{ mV/MPa}$ . The hydrophone directivity at 1.5 MHz was measured separately and used to provide corrections for improved accuracy. Hydrophone location was controlled using 3-D positioner systems based on stepper motors and linear slides with resolutions less than  $10 \mu\text{m}$  per step (Velmex Inc., Bloomfield, NY, USA).

A function generator (Model 3500B, Keysight Technologies, Inc., Englewood, CO, USA) was used to trigger the VDAS and synchronize data acquisition on an oscilloscope or digitizer. For the holography scan, hydrophone signals were recorded using a 14-bit digitizer board (Razor 14, Gage by DynamicSignals LLC, Lockport, IL, USA); for other experiments, hydrophone measurements were recorded using a digital oscilloscope (Model 3034A, Agilent Technologies Inc, Santa Clara, CA, USA).

The angular sensitivity response of the hydrophone was measured up to an angle of  $40^\circ$  in an open water bath in the far field of a 1.5-MHz flat piezoelectric source with 1.6 cm diameter. The response was measured along four different azimuthal angles by rotating the hydrophone around its axis and repeating the measurements twice for each angle. The average of these measurements at each angle was then taken to produce the angular response curve shown in Fig. 2.

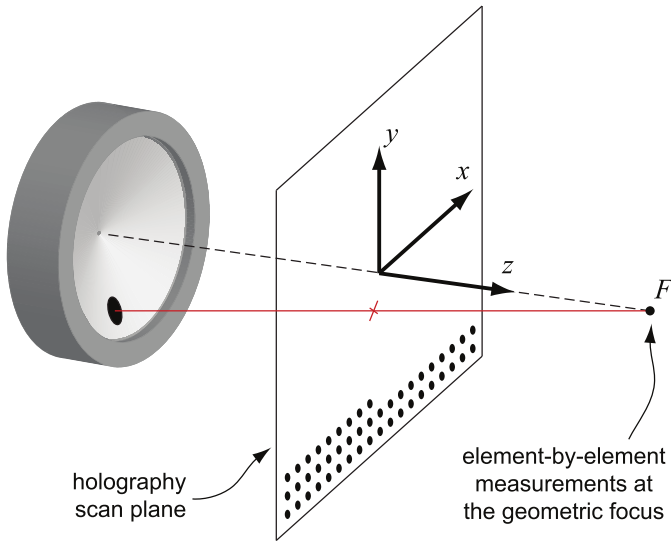


Fig. 3. Diagram of the experimental setup. The acoustic focus (F) at which element-by-element hydrophone measurements were taken was determined as a maximum of pressure amplitude when all elements were triggered simultaneously. The holography scan plane with an area of  $88 \times 88 \text{ mm}^2$  was 40 mm prefocally. The hydrophone recorded the waveform at 0.5-mm increments for a total of 31 329 points. Sample points shown as dots are at larger increments for illustration.

Based on the small variation, the curve is assumed axisymmetric. The acoustic characterization section of this paper reports various acoustic output and efficiency measurements after compensation for the hydrophone's angular response while a comparison to the values before compensation are reported in the discussion.

Losses due to absorption of the fundamental frequency (1.5 MHz) were ignored in the analysis since they were negligible (0.054 dB over the longest propagation distance to the acoustic focus of 120 mm). Nonlinear propagation effects were neglected in all acoustic measurements. Focal measurements were performed at low voltage levels while holography and RFB measurements were performed prefocally. The level of the second-harmonic pressure was less than 7% in all measurements, yielding an intensity level less than 0.5%, which is below the nonlinear intensity threshold criterion of 10% in standards [34].

1) *Far-Field Element-by-Element Measurements*: In the element-by-element measurements, the hydrophone was placed at the acoustic focus of the phased array, which is in the far field of all elements (Fig. 3). The focus of the array was determined as the location where the hydrophone recorded the maximum pressure amplitude while all elements were driven at the same voltage level and without applying any phase delays. Each element was then driven independently at 1.5 MHz with a 128-cycle burst. The waveform was recorded, and the amplitude and phase were calculated using a discrete Fourier transform (DFT) over the steady state portion of the waveform. The continuous wave (CW) boundary condition (pressure) at each element surface was then estimated by assuming each element can be modeled as a flat, circular piston source with a uniform normal velocity  $v_0 = P_0/\rho c$ . In the

far-field approximation

$$P_0 = P_R \frac{R\lambda}{\pi a^2} \quad (2)$$

$$W = P_R^2 \frac{R^2 \lambda^2}{2\rho c \pi a^2} \quad (3)$$

where  $P_0$  is the effective surface pressure amplitude,  $P_R$  is the pressure amplitude measured at the focus after applying relevant correction for directivity. Considering that the hydrophone was aligned with the array axis, the angle of incidence was determined as the angle between the array axis and the vector defined by the location of an element of interest relative to the hydrophone. Then, the corresponding relative amplitude of the directional response was used to apply a correction.  $R$  is the focal distance,  $a$  is the nominal radius of each element,  $W$  is the acoustic power of the (piston) array element,  $c$  is the speed of sound in water,  $\rho$  is the density, and  $\lambda$  is the ultrasound wavelength. Based on the measurements for each element, the total acoustic power output and the overall transducer efficiency were calculated.

2) *Acoustic Holography*: In the holography scan, all elements were driven simultaneously with a 128-cycle burst. Hydrophone signals were acquired at each location over a 2-D plane oriented approximately perpendicular to the acoustic axis. The scan was performed with the center of the scan region located 40 mm proximal to the transducer relative to the acoustic focus (Fig. 3). The scan comprised an  $88 \times 88 \text{ mm}^2$  grid with a step size of 0.5 mm. From the recorded hydrophone signals, the CW hologram was defined by analyzing a time window lasting for 15 acoustic cycles with a delay time of  $111.17 \mu\text{s}$  after triggering, and calculating pressure amplitude and phase of the windowed signal using DFT. The time window was chosen based on a VDAS delay of  $2.17 \mu\text{s}$  before actual waveform generation, a delay for acoustic propagation from each element to each point within the scan plane, and a transient ring-up time for the array to reach a steady state. Using the angular spectrum calculated from the raw holography measurements, we compensated for the hydrophone directivity and then calculated the power traversing the scan plane [35] using the following relations:

$$S(k_x, k_y) = \iint P(x, y) e^{-ik_x x - ik_y y} dx dy \quad (4)$$

$$\tilde{S}(k_x, k_y) = \frac{S(k_x, k_y)}{D(\theta(k_x, k_y))} \quad (5)$$

$$W = \frac{1}{8\pi^2 \rho c} \iint_{k_x^2 + k_y^2 \leq k^2} \sqrt{1 - \frac{k_x^2 + k_y^2}{k^2}} |\tilde{S}(k_x, k_y)|^2 dk_x dk_y \quad (6)$$

where  $S(k_x, k_y)$  is the measured angular spectrum of the beam,  $k_x$  and  $k_y$  are the wave vector components in  $x$  and  $y$ ,  $P(x, y)$  is the measured complex amplitude of the pressure field,  $D(\theta)$  is the directivity, and  $\theta$  is related to  $k_x$  and  $k_y$  by  $\sin \theta = (k_x^2 + k_y^2)^{1/2}/k$ .

After compensation for the angular response of the hydrophone, the inverse Fourier transform was used to recover the true complex pressure amplitude distribution from the

recovered angular spectrum using the following expression:

$$\tilde{P}(x, y) = \frac{1}{4\pi^2} \iint \tilde{S}(k_x, k_y) e^{ik_x x + ik_y y} dk_x dk_y. \quad (7)$$

When considering the holography measurements and the physical transducer, there are two relevant coordinate systems: one aligned with the transducer and the corresponding beam's  $z$ -axis, and another aligned with the axes of the hydrophone positioner ( $x, y, z$ ). The acoustic beam  $z$ -axis is not generally coincident with the hydrophone  $z$ -axis [31], but the misalignment can be corrected by projecting the field to different transverse planes in the positioner coordinates and identifying movement of the beam axis relative to these coordinates. After quantifying the misalignment in this way, a transformation basis between the positioner and transducer coordinates was defined, and the measured hologram was interpreted accordingly. For simplicity, in figures 4, 5, 8 and 10 presented in this paper, all coordinates ( $x, y$ ) shown are either describing hydrophone axes if shown in a focal plane, or array axes if shown on the array surface.

After the alignment of coordinates, the pressure field recovered from the inverse transform (7) was used to back project the field to a spherical surface that corresponded to the physical surface of the transducer using the Rayleigh integral [31]. From reconstructed normal velocities of the transducer surface, the preliminary boundaries of individual elements were identified based on the maximum of the gradient of velocity amplitude along the transducer surface. Afterward, the surface normal velocity profile was manually inspected to remove spurious pixels connecting adjacent elements. The pixels inside each boundary were then used to define the corresponding element's central location as the centroid of these pixels. Final-element boundaries were drawn around each of these calculated locations as 7-mm-diameter circles to agree with reported manufacturer specifications. The information inside each element's boundary was collected to calculate its acoustic output as follows:

$$A_j = \frac{1}{N} \sum_{i=1}^N A_{ij} \quad (8)$$

where  $A_j$  is the complex amplitude either of normal velocity or pressure per element  $j$ , and  $N$  is the number of pixels with their centroid inside an element. The power emitted by the element  $j$  is  $W_j = (1/2) \sum_{i=1}^N \text{Re}(P_{ij}^* U_{ij}) \times da_i$ , where,  $da_i$  is the projection of the square surface area of pixel  $i$  onto the spherical array surface, and  $P_{ij}$  and  $U_{ij}$  are the complex amplitudes of pressure and normal velocity, respectively.

3) *Radiation Force Balance Measurements*: RFB measurements were carried out using a flat 10-cm-diameter absorber brush [36] suspended from a precision scale (Entris623i-1S, Sartorius, Göttingen, Germany) and placed 1 cm proximal to the acoustic focus. A 50- $\mu\text{m}$ -thick Mylar membrane was placed between the transducer and the absorber to minimize acoustic streaming [37], and the transducer was operated at a 1% duty cycle to minimize heating of the absorber [38]. Based on the ray acoustics theory [39], the following correction factor was multiplied by the acoustic power to correct for the

geometry of a focused source with a central hole

$$\text{C.F.} = 2/(\cos \alpha_1 + \cos \alpha_2) \quad (9)$$

where  $\alpha_1$  and  $\alpha_2$  are the angles which correspond to half apertures of the central opening and the outer edge of the array.

4) *Equalization of the Output of the Array Elements (Uniformity)*: Equalizing the element outputs includes phase corrections to have all elements firing in phase and amplitude equalization. In order to find the phase delays among the elements for the element-by-element measurements, the recorded signal of each element was used to calculate the relative phase delay between the elements. For the holography scan, the phase delays among elements were found using the phase values from the complex normal velocity of each element given by (8). Phase delay corrections were then applied to the VDAS for both measurements.

Then, a VDAS apodization scheme was used to equalize the element amplitude outputs by controlling the voltage delivered to each element. The VDAS takes an apodization factor as input and uses pulsewidth modulation to control the number of "ON-" and "OFF-" clock cycles in a transmit event to set the voltage amplitude on a specific channel. In order to measure the relative electrical output versus the apodization factor applied in the VDAS script, the voltage was measured on a single element for apodization factors ranging from 0 to 1 in increments of 0.1, where 0 denotes being fully OFF and 1 denotes being fully ON. To obtain the required driving voltage for each element from both characterization methods, the reciprocals of effective normal velocity amplitudes from element-by-element measurements and the reciprocals of surface normal velocity amplitudes from holography were found and normalized relative to the largest value of each method separately. The normalized reciprocals were used as scaling factors to control the voltage output delivered to each element, such that the lowest element was scaled by unity and the rest by a factor less than 1. Then, the scaling factors were used back to solve and determine the required apodization factors applied in the VDAS script to control the voltage delivered to the elements and ultimately equalizing the amplitude outputs.

5) *Generation of Vortex Beams*: Vortex beams with topological charges,  $M = 0$  (focused), 1, and 4, were generated after applying amplitude and phase corrections, in order to test the effectiveness of the characterization methods for achieving uniformity of the beams. We ran the VDAS script with the relevant apodization factor for each element to equalize amplitudes. In addition to equalizing phase delays, further phase delays were imposed to synthesize different vortex beams. The phase delay imposed on each element was calculated based on its nominal location ( $x_i, y_i$ ). For a given  $M$ , the total phase delay around the array aperture increases from 0 to  $2\pi M$ , and the phase on element  $i$  is given by

$$M \times \arctan(y_i/x_i). \quad (10)$$

The 2-D hydrophone scans of multiple vortex beam shapes in the focal plane were measured before and after the application of equalization corrections. Pressure amplitude and phase were

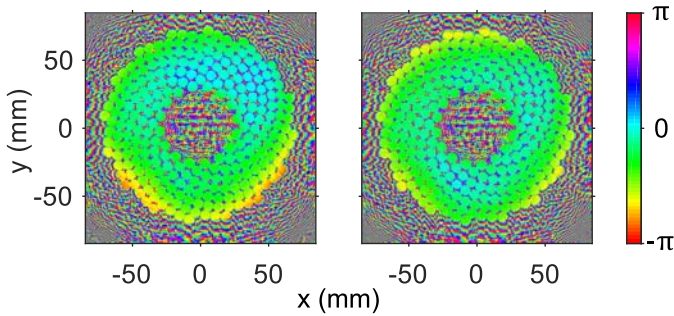


Fig. 4. Phase distribution (radians) back projected onto the transducer surface before (left) and after (right) correcting for the misalignment of the array and holography coordinates. Before correction, the slight misalignment is observed as a nonuniform phase distribution varying from top to bottom on the array surface.

calculated from waveforms recorded at each spatial location in the scan, as described for the holography scan.

The intensity calculated from measurements was then compared to the simulated intensity to evaluate the performance of the characterization methods. Simulations used the Rayleigh integral to calculate pressure fields that would be generated by an idealized representation of the array—uniformly vibrating elements were assumed, with element locations and sizes matching manufacturer specifications.

### III. RESULTS

#### A. Element-by-Element in the Far-Field Measurements

Using the recorded pressure waveform for each element, the effective pressure amplitude and phase at the element's surface were found and then used to calculate the radiated acoustic power from (2) and (3). For all elements, the total acoustic power was calculated to be 91.4 W. The applied electrical power was 136.4 W yielding an efficiency of 65.5%, which falls within the specifications provided by the manufacturer.

#### B. Holography

The holography results are presented to show the alignment of the axes, the element locations and borders, the effect of the directivity on the surface normal velocity vibration profile, and finally the acoustic power output and efficiency calculations.

1) *Holography Axes Alignment*: Before using the measured hologram to reconstruct vibrations on the transducer's surface, corrections were performed for misalignment between the hydrophone and the transducer coordinates. The uncertainty in the alignment of the acoustic beam axis with the  $z$ -axis of the 3-D positioner was found by forward projecting to the focal plane away from the array. The focus appeared to be located at (0.15, -0.25) mm rather than at (0, 0). Using this offset from the origin over the propagating distance ( $\delta z = 40$  mm), the misalignment angle between the axes was found to be  $0.42^\circ$ . After correcting for the angular misalignment and back projecting to the array surface, a more uniform phase distribution was obtained (Fig. 4). This misalignment only affects the surface phase distribution and has no visible effect on the amplitude.

2) *Element Locations and Sphericity*: Element locations identified from reconstructed vibrations at the transducer surface were compared to the nominal locations provided by the manufacturer. To perform this comparison, we note that the orientation of array elements around the beam axis was not controlled relative to any absolute coordinate system. Accordingly, the holographically reconstructed element positions were rotated around the beam axis for initial alignment relative to the manufacturer-specified coordinates. Then, an iterative algorithm was executed to optimize alignment by minimizing the sum of the absolute differences between nominal and reconstructed element locations. The minimization search was carried out by first rotating the holographically reconstructed array pattern in the  $xy$  plane about the  $z$ -axis. Second, this pattern was shifted in the  $xy$  plane while conserving the radius of curvature of the surface, where the vibration velocity pattern was reconstructed. These two steps were repeated iteratively using an angular search with a step size of  $0.001^\circ$  from  $-5^\circ$  to  $5^\circ$  and a translational search with a step size of 0.001 mm from  $-2$  to 2 mm. The optimal alignment found in this way yielded an average distance between nominal and reconstructed locations of 0.107 mm with a standard deviation of 0.055 mm. In addition, the diameter of each reconstructed element was found to be 6.99 mm with a standard deviation of 0.2 mm, which agrees with the nominal element's diameter of 7 mm.

From this alignment comparison, an interesting characteristic of the transducer's acoustic surface was identified. In particular, it appears that the transducer was made from two physically separate halves that were joined together in the manufacturing process. The line representing that split in the transducer surface was captured by the holography results illustrated in Fig. 5, which shows the surface normal velocity profile after directivity compensation along with the identified element boundaries shown in white.

3) *Acoustic Output and Efficiency Calculations*: The normal velocity output and acoustic power per element were calculated from (8). The acoustic power from the measured hologram in the scan plane was 308.9 W. After performing back projection to the transducer surface and localizing the output per each element, the sum of the acoustic power from all elements was 301 W. Although no absorption losses were included in back propagation, the difference of 2.53% of the total power was from including only radiation from inside the 7-mm element boundaries.

In Fig. 2, it is shown that the angular response was measured up to  $40^\circ$ ; however, the maximum angle the hydrophone reached with the transducer in the holographic scan was  $50^\circ$ . The sensitivity past  $40^\circ$  was assumed to be linearly decreasing down to a value at  $90^\circ$  equal to 8% of the value at  $40^\circ$ . The linear curve is defined to be a lower bound to the theoretical sensitivity value specified by the manufacturer and given by the expression for a radiating source in free space in [40]. For verification purposes, we compared the power values gained from using the linear curve—a lower bound—against an assumed constant sensitivity curve beyond  $40^\circ$ —an upper bound—as the most conservative limit. The acoustic power was measured to be 306.3 and 308.9 W for constant and

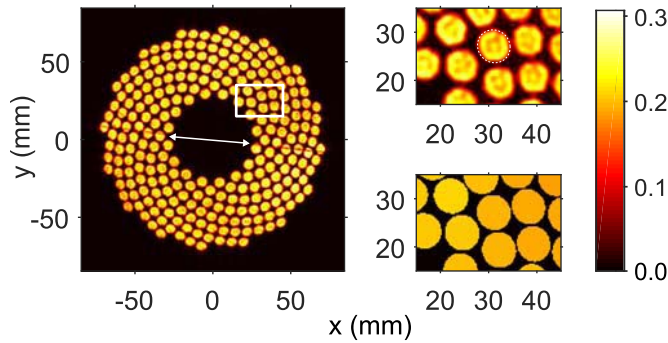


Fig. 5. (Left) Transducer's surface normal velocity amplitude profile,  $|U|$  (m/s), obtained with compensation for the hydrophone directivity. The arrow marks the line along the hemispherical surface splitting the transducer surface into two halves due to the manufacturing process. (Right) Close-up of the elements in the upper right corner of the array; (top) surface normal velocity amplitude profile,  $|U|$  (m/s), with an example of the calculated boundaries of the elements shown as a dashed contour on a single element, and (bottom) averaged and localized surface normal velocity amplitude,  $|U|$  (m/s), per element after postprocessing of the holography results. Note that the reconstructed surface normal velocity (top) is not uniform within each element which may be explained not only by some true heterogeneity of the source vibration, but also by the omission of evanescent wave components in the far-field holography reconstruction used.

linear directivity curves, respectively, which is an increase of less than 1%. The electrical power was calculated to be 463.2 W, which resulted in efficiency values between 66.1% and 66.7%, depending on which the directivity curve was used. This estimation beyond  $40^\circ$  was not required for the element-by-element, since the hydrophone was placed in the focus, making a maximum angle with the outermost transducer elements less than half the focal angle of  $37^\circ$ .

Element-by-element measurements were performed at 55% of the driving voltage of holography, yielding an electrical power of 136.4 W. Holography required higher voltage levels to obtain a good signal-to-noise ratio, since the hydrophone was placed 40 mm prefocally (averaging would have prolonged the scan time considerably). Moreover, making element-by-element measurements at the drive level used for holography was not performed in order to avoid exposing the hydrophone to high pressures at the focus.

### C. Radiation Force Balance Measurements

An RFB was employed to provide an independent measure of acoustic power. To eliminate potential inconsistencies introduced by the driving electronics, the input electrical power was measured and used to normalize these acoustic power measurements in terms of overall transducer efficiency. The acoustic power measured at the voltage level of the holography scan was 315.8 W. The average efficiency calculated from RFB measurements at different voltage input levels was 68.3%, while the efficiency calculated from the holography scan (66%), element-by-element measurements (65.5%) and manufacturer's reported efficiency ( $>63\%$ ). The reported efficiency by the manufacturer was calculated using 32 central elements only rather than the whole array. However, our measurements indicate that the outer elements have efficiencies similar to the inner 32 elements.

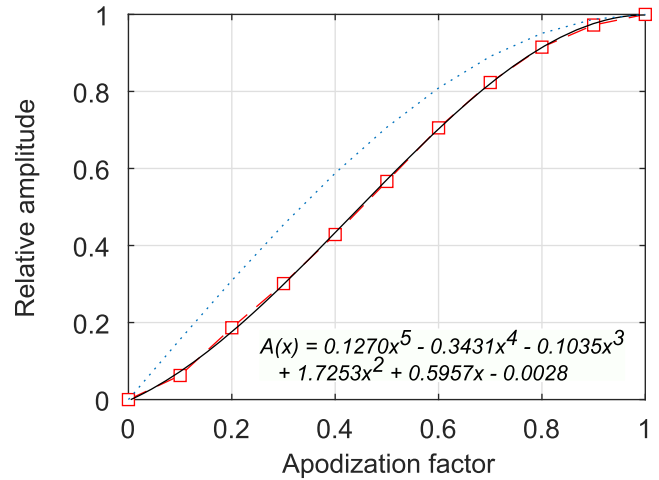


Fig. 6. Apodization factor versus relative amplitude output of the VDAS for an extended burst for all elements firing simultaneously. The red dashed curve represents the measurement results and their fifth-degree polynomial fit (black solid line); both compared with the pulsewidth modulation scheme assuming a sinusoidal curve (dotted blue line). The fifth-degree polynomial fit is displayed with restriction of having a value of zero at zero and unity at one.

### D. Equalizing the Output of the Array Elements

The VDAS apodization factor versus the voltage output amplitude was measured (Fig. 6). Since the VDAS apodization factor ( $A_p$ ) indicates full power when equal to unity and OFF when zero, it would be theoretically expected for the resulting amplitude of the output to follow a sinusoidal curve,  $\sin((\pi/2)A_p)$ , where  $A_p$  is the apodization factor varying from zero to unity. However, measurement of the voltage amplitude output versus various apodization factors showed deviation from this curve that could be a result of multiple sinusoidal summations, and thus the curve was approximated by a fifth-degree polynomial using a least-squares fit. The polynomial curve was used to calculate the desired apodization factor to equalize all elements' amplitude outputs based on the element-by-element and holography results (Fig. 5). Phase corrections based on both methods were applied to have zero relative phase delay between all elements.

The pulsewidth modulation scheme in the VDAS is constrained since it is only possible to specify an integer number of "ON" cycles in a half-transmit clock. This constraint on temporal resolution limits the resolution with which each element's amplitude can be controlled. Fig. 7 shows the desired relative amplitude value (black solid line) versus the VDAS output (red dashed line). As can be seen, the discretization of output levels for some elements causes a nonideal equalization of the array.

### E. Generation of Vortex Beams

The 2-D scans were performed in the focal plane of beams with multiple topological charges ( $M = 0, 1, \text{ and } 4$ ) as generated with and without equalization of element outputs. From such measurements, the performance of equalization based on each characterization method was quantified by comparison with idealized simulations. A performance metric

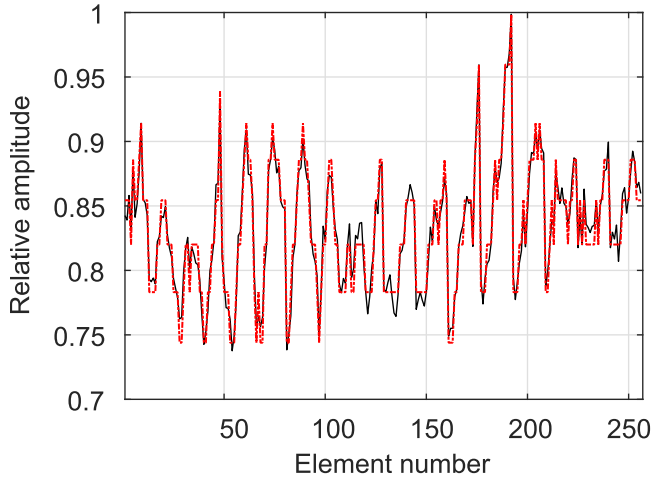


Fig. 7. Effect of VDAS rounding to whole integers in defining the number of “ON-clock” cycles in the apodization scheme. VDAS rounds up or down to the nearest integer to define the number of “ON-clock” cycles in the apodization scheme, which limits control of the resolution of the desired output as it underestimates or overestimates the needed amplitude. The VDAS output (black solid line) is shown to deviate from the desired output (red dashed line).

TABLE II  
RELATIVE ERROR NORM OF INTENSITY OF ACOUSTIC  
BEAM SHAPES BEFORE AND AFTER EQUALIZATION

Topological charge ( $M$ )	Before equalization	Element-by-element equalization	Holography equalization
0	10.1%	15.3%	9.0%
1	10.8%	9.1%	5.3%
4	13.3%	7.8%	7.4%

was calculated based on error in the intensity distribution relative to the corresponding simulation as follows:

$$E = \frac{\sum \sum |I(x, y) - I_s(x, y)| dx dy}{\sum \sum I_s(x, y) dx dy}$$

where  $I_s$  is the 2-D intensity distribution from simulation and  $I$  is the 2-D intensity distribution—normalized with respect to the total power in  $I_s$ —from before or after equalization as obtained by either element by element or holography.

Fig. 8 shows the normalized intensity distributions corresponding to measurements in the scan plane and corresponding simulation results. All the vortex beam shapes scanned had the same input electrical power; however, the acoustic energy captured in the section of the scan plane shown in Fig. 8 varied slightly with the apodization factors from each method. Therefore, all intensity scans in Fig. 8 are normalized to the acoustic power in the scan plane of the simulation results to calculate the relative error.

Table II presents errors associated with array nonuniformity as calculated from the intensity distributions in Fig. 8. Fig. 8 and Table II show that both element-by-element measurements and holography attain improved uniformity for higher values of topological charge  $M$ . Values for  $M = 0$  show that element-by-element equalization performs worse than no equalization—15.3% versus 10.1%,

while holography equalization provides minimal improvement. However, Fig. 8 illustrates that both equalization methods yield more circular intensity distributions with the element-by-element method providing the narrowest focal region. Overall, holography outperforms element-by-element measurements and reduces intensity nonuniformity by a factor of about 2 relative to the case with no equalization.

Sectional cuts along the  $x$ -axis for  $M = 0$ , and circumferential cuts at the radial distance with the maximum intensity values for  $M = 1$  and 4 from the simulation were also examined for comparison of the performance of different equalization methods (Fig. 9). In a fashion similar to Table II, the residual relative percent error is plotted in Fig. 9 along the black dashed lines shown in the right-hand column of Fig. 8.

Both equalization schemes improved the intensity distribution for most cases (Figs. 8 and 9). For  $M = 0$  in Fig. 9, the peak intensity obtained using both equalization methods (black and red dashed lines) is higher relative to the simulated data ( $y = 0$ ) because it has a wider distribution of intensity than the measured cases, while the power in all beams is the same. Circumferential cuts for  $M = 1$  and 4 show the overall improvement in uniformity between the spatial distribution. For instance, at  $M = 1$  from the holography method, the residual error is generally less than that from far-field measurements with the error oscillating between 0% and  $-5\%$  except a large peak of 10% at  $\theta = 125^\circ$ . Similarly, for  $M = 4$  holography exceeds element-by-element measurements, only underperforming on the interval from  $\theta = 160^\circ$  to  $195^\circ$  and  $0^\circ$  to  $50^\circ$ . Interestingly, a close inspection of Fig. 9 shows the effect of the equalization scheme on the extreme of the nonequalized case. It is noticeable that uniformity is improved as spatial extrema are flattened. However, there are areas where a maximum or a minimum was overcompensated for, such as at  $\theta = 285^\circ$  for  $M = 1$  or  $\theta = 150^\circ$  for  $M = 4$ . Similar to the 2-D intensity plots of Fig. 8 and the error percent calculated in Table II, the radial cuts of Fig. 9 display more regions of high nonuniformity distribution from simulation are present in the equalization results of the element by element than the holography method.

The phase distribution of various vortex beam shapes was measured to quantify the uniformity of the source before corrections. The distribution was plotted before and after applying corrections. The phase distribution before corrections (second column of Fig. 10) shows slight variations along the radial direction inside the main circular boundary. In addition, at  $M = 4$ , nonideal phase distribution is observed. Such results are the consequence of small disturbances in the field introduced by the nonideality of the source. For instance, due to manufacturing errors and tolerances, the array deviates from an ideal spherical surface. Such deviations introduce small perturbations in the acoustic field which lead to instabilities in the low amplitude regions of vortex beams with  $M > 1$ , as has been shown in optics [41]–[43]. Furthermore, for elements intended to have the same phase, a maximum time delay of 3 ns was measured before applying phase corrections. Such a small value indicates that the transducer’s elements are well

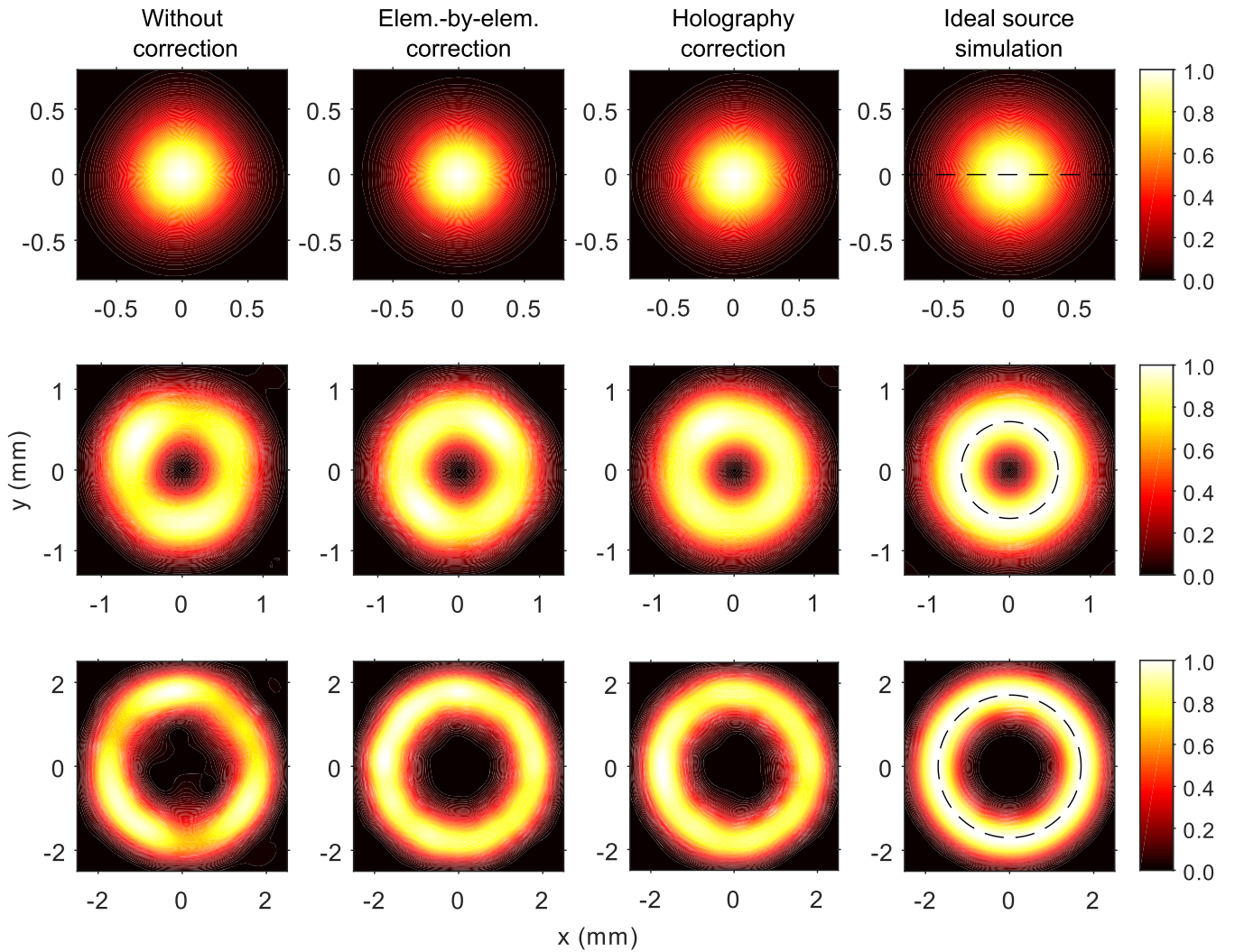


Fig. 8. Normalized 2-D intensity distribution to its maximum value in the focal plane for different  $M$  values:  $M = 0$  (top),  $M = 1$  (middle), and  $M = 4$  (bottom), for (from left to right) measurements before and after apodization using element-by-element measurements and holography results, and simulation. The corrections improve the uniformity of the focal rings and final experimental results look more like the simulation. The dashed line in the left column shows the line along which the sectional and circumferential cuts were taken for use in Fig. 9.

within the phase of each other and the jitter in phase between them is negligible.

To find the contribution of the amplitude equalization and phase corrections to the uniformity, the results of elements' output obtained from holography were used to simulate the beam shapes applying no corrections, amplitude equalization only, or phase corrections only. The three simulation cases were compared to simulation with ideal phase and amplitude, and the error in the intensity distribution was quantified, and the results are presented in Table III. First, the simulation results before equalization from Table III agree with the measurements of the fields before equalization in Table II. Also, Table III illustrates that the contribution of the nonequal element amplitude outputs has the largest error contribution of 6.3% at  $M = 0$ , then it steadies at larger  $M$  values to around 4%. Conversely, the phase error contribution increases with larger  $M$ , since at higher  $M$  the increment change in phase delay between elements to produce a specific vortex

TABLE III  
COMPARISON OF ERROR NORM OF SIMULATION OF INTENSITY OF ACOUSTIC BEAM SHAPES FROM HOLOGRAPHY RESULTS WITH EITHER AMPLITUDE EQUALIZATION OR PHASE CORRECTIONS

Topological charge ( $M$ )	Before equalization	Amplitude equalization only	Phase corrections only
0	10.4%	9.6%	6.3%
1	10.8%	9.9%	4.2%
4	15.3%	14.5%	4.4%

beam approaches the inherent phase errors of the array elements.

#### IV. DISCUSSION

In this paper, a high intensity focused ultrasound transducer was characterized using two well-known methods, holography and element-by-element measurements. Both approaches were

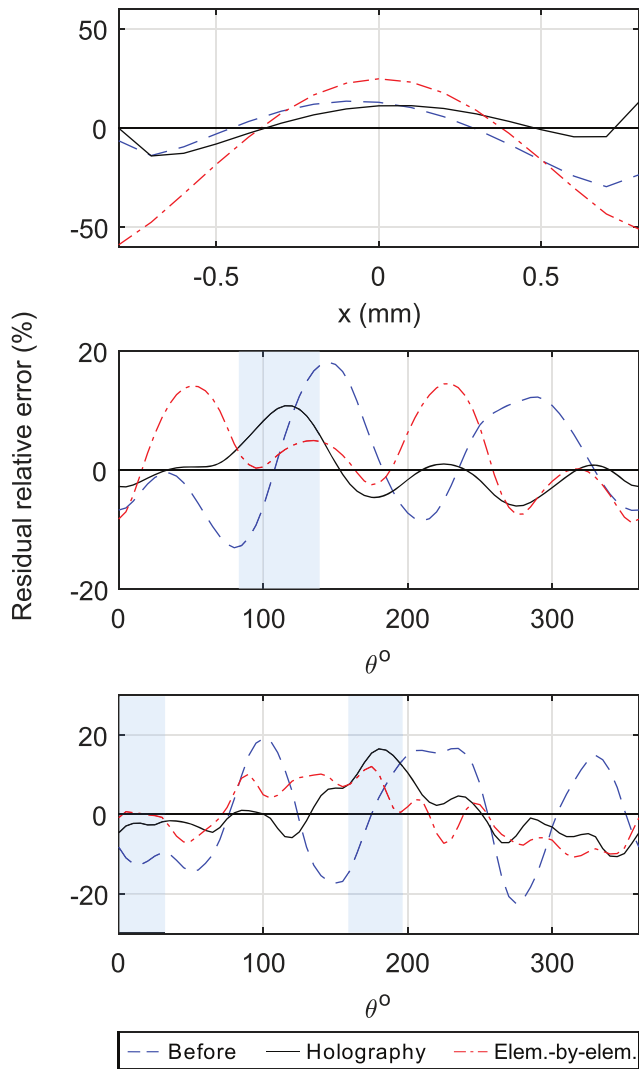


Fig. 9. Sectional and circumferential cuts of residual relative error (%) to the simulation of an ideal array output for  $M = 0$  (top),  $M = 1$  (middle), and  $M = 4$  (bottom). Sectional cut is taken along the  $x$ -axis for  $M = 0$  (top), and circumferential cuts are taken at the radius with the maximum intensity value for  $M = 1$  and  $4$  (middle and bottom, respectively). Shaded areas for  $M = 1$  and  $4$  highlight the sections where holography underperforms element-by-element measurements.

used to estimate the complex pressure and normal velocity of each element, including both amplitude and phase. These characterization measurements were then used to modify how each element was driven in order to equalize element outputs. The performance of equalization based on both holography and element-by-element measurements was evaluated by generating vortex beams and comparing the resulting intensity distributions with simulations representing an idealized array.

Measurements of vortex beams show that equalization of element outputs improved beam uniformity for all shapes, except for the focused case of element by element even though it produced more circular intensity distribution than before. While the comparison of phase distributions suggests excellent uniformity across all array elements, some nonuniformities in measured beams are still evident, which may be attributable to various sources including discretization error in the VDAS apodization routine, which was estimated to contribute less

than 1.9% change in the pressure field. This effect could be potentially improved or eliminated by electronically matching each element separately; however, as a practical tradeoff we did not pursue this level of complexity.

In general, the 2-D scans of acoustic beams from the element-by-element method exhibit greater nonuniformity and different intensity distributions than those from holography. There are two factors causing this additional nonuniformity. First, element-by-element measurements are taken at the focus, and unlike holography, these measurements do not characterize the surface vibration profile and instead record a far-field approximation of the effective pressure amplitude on the element. Second, electrical variability was present in the VDAS driving system. In our configuration, it was measured that the VDAS will deliver when all elements are operating simultaneously 84% of the voltage compared to when a single element is driven. Furthermore, because of the power drainage behavior of the capacitors in the VDAS and transient response of the external power source used, the output response among the elements, when firing one element at a time, can vary if they are driven one after another at a high pulse frequency rate. Therefore, in the element-by-element experiment, the elements were triggered at 1-Hz frequency to allow the power source to recover between pulses and eliminate this variability when measuring and recording the relative amplitude information. Conversely, if all elements are triggered simultaneously, the total output of the array can change based on the pulse rate frequency; however, the output of the elements relative to one another is steady. Thus, the holography 2-D scan in this situation was necessary to capture the actual operating conditions and eliminate this additional electrical variability.

A 2-D holography scan has many advantages over element-by-element measurements, such as characterizing the acoustic output of all elements synchronously, obtaining the surface boundary conditions, which can be used to produce any arbitrary 2-D field shape and capturing other details about the array geometry, layout, and imperfections. However, there were several limitations in the 2-D holography scan that were not addressed in the analysis presented. The scan lasted for several hours over which the water temperature changes, thus leading to a change in the acoustic properties of the medium, hydrophone sensitivity response, and heating of electrical components. During our scan, the temperature changes in water were limited to  $1\text{ }^{\circ}\text{C}$ – $2\text{ }^{\circ}\text{C}$ . Furthermore, even though the misalignment of coordinates was corrected for, nonorthogonality between the mechanical axes can contribute to holographic reconstruction errors. These errors are additional contributing factors to the presence of nonuniformity in the distribution after equalization. Reference [31] presents a detailed discussion of the contribution of each source of error to the reconstruction results.

Although known and required in standards [44], the hydrophone directivity had a significant effect on the power measurements. Therefore, a curve fit using the directivity of a source radiating in free space [40] was performed on the directivity results and yielded an effective element size of  $510\text{ }\mu\text{m}$ , which is over twice the nominal size of  $200\text{ }\mu\text{m}$ . For element-by-element measurements, accounting for directivity increased

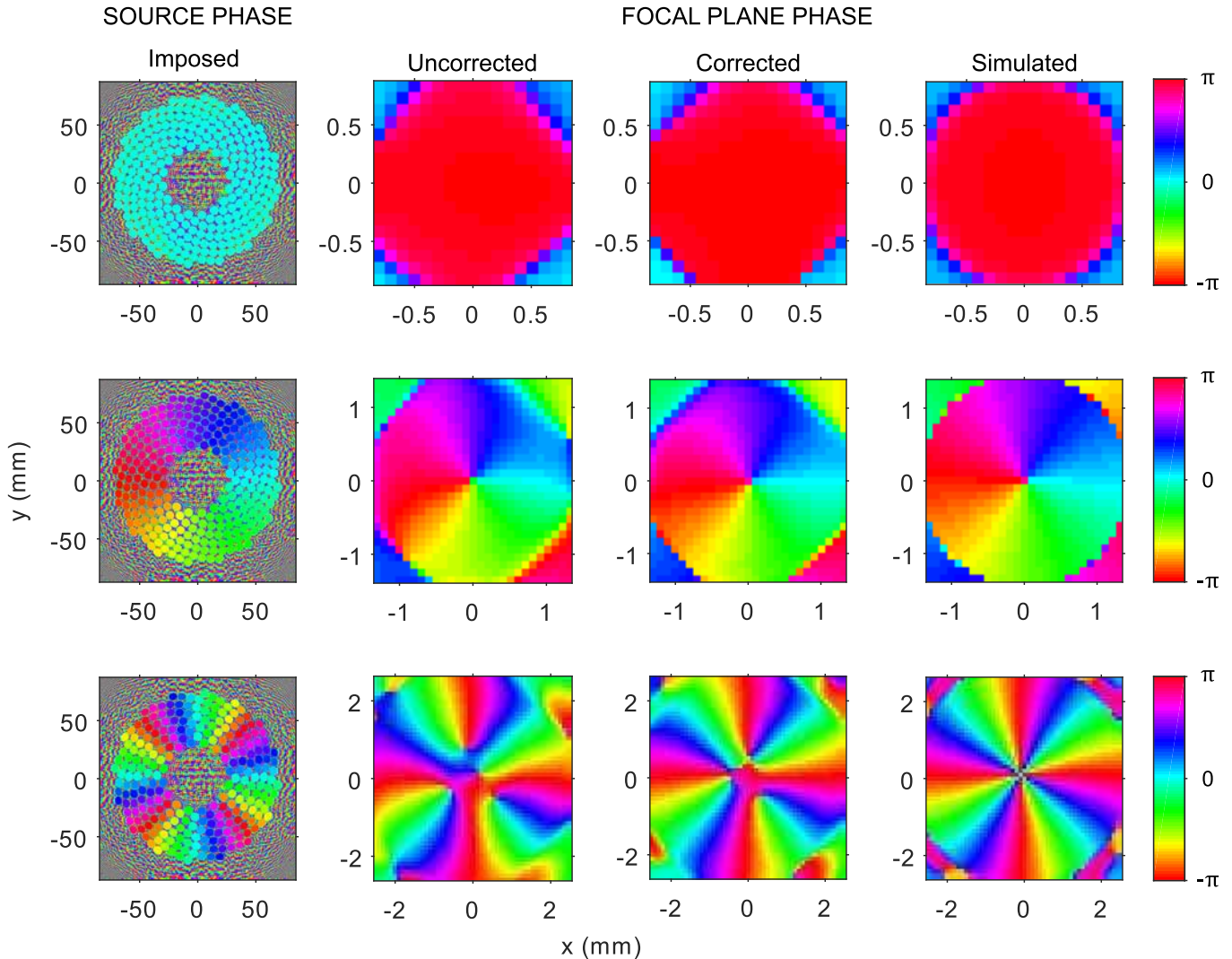


Fig. 10. Phase distribution of vortex beams (radians). Imposed phase distribution on the array's discrete elements, measured phase distribution at the focal plane before and after applying phase corrections (left–right), and simulation for  $M = 0, 1,$  and  $4$  (top–bottom). Before applying phase corrections, there are slight variations in the phase distribution along the radial direction. The smooth phase transition indicates that the array behaves as a continuous acoustic source.

the power from 72.5 to 91.4 W, a 26.1% increase; for holography measurements, consideration of directivity increased power from 245.8 to 308.9 W, a 25.7% increase. Furthermore, even though we measured the directivity up to  $40^\circ$  and the hydrophone reached a maximum angle of  $50^\circ$  during the scan, it was shown that maximum possible power contribution with the most conservative comparison is 1%, leading to the conclusion that for such a focused array majority of the acoustic power lies within the aperture angle of the array.

## V. CONCLUSION

A 256-element array system was characterized in this paper. Element outputs were equalized and the ability to generate uniform vortex beams that potentially could be used for the acoustic manipulation of kidney stones was demonstrated. The acoustic output of the phased array was successfully characterized by performing element-by-element and holography measurements. The element-by-element method was used to find the effective pressure amplitude and relative phase delay of each array element. For the first time to our knowledge, each

element's output was localized in a holographic reconstruction at the transducer's surface, with the corresponding power attributed to localized elements equal to 97.5% of the total radiated power. The output was successfully equalized to produce uniform vortex beams in the focal plane. Measurements of uniformity of the beam intensity distribution showed that equalization based on holography surpassed that based on element-by-element measurements. While some nonideal behavior persisted, the system was sufficient to accurately produce vortex beams. This method paves the way for the future synthesis of more complex 2-D beams for acoustic manipulation.

## ACKNOWLEDGMENT

The authors would like to thank their colleagues of the Center for Industrial and Medical Ultrasound, University of Washington, Seattle, WA, USA. The authors would also like to thank the Laboratory for Industrial and Medical Ultrasound, Moscow State University, Moscow, Russia.

## REFERENCES

- [1] D. Foresti, M. Nabavi, M. Klingauf, A. Ferrari, and D. Poulikakos, "Acoustophoretic contactless transport and handling of matter in air," *Proc. Nat. Acad. Sci. USA*, vol. 110, no. 31, pp. 12549–12554, 2013.
- [2] Y. Ochiai, T. Hoshi, and J. Rekimoto, "Pixie dust: Graphics generated by levitated and animated objects in computational acoustic-potential field," *ACM Trans. Graph.*, vol. 33, no. 4, 2014, Art. no. 85.
- [3] A. Marzo, S. A. Seah, B. W. Drinkwater, D. R. Sahoo, B. Long, and S. Subramanian, "Holographic acoustic elements for manipulation of levitated objects," *Nature Commun.*, vol. 6, p. 8661, May 2015.
- [4] J. D. Harper *et al.*, "First in human clinical trial of ultrasonic propulsion of kidney stones," *J. Urol.*, vol. 195, no. 4, pp. 956–964, 2016.
- [5] A. Shah *et al.*, "Novel ultrasound method to reposition kidney stones," *Urol. Res.*, vol. 38, no. 6, pp. 491–495, 2010.
- [6] P. C. May, M. R. Bailey, and J. D. Harper, "Ultrasonic propulsion of kidney stones," *Current Opinion Urol.*, vol. 26, no. 3, pp. 264–270, 2016.
- [7] B. Hefner and P. Marston, "An acoustical helicoidal wave transducer with applications for the alignment of ultrasonic and underwater systems," *J. Acoust. Soc. Amer.*, vol. 106, no. 6, pp. 3313–3316, 1999.
- [8] J. Arlt and K. Dholakia, "Generation of high-order Bessel beams by use of an axicon," *Opt. Commun.*, vol. 177, no. 1, pp. 297–301, 2000.
- [9] R. Marchiano and J.-L. Thomas, "Synthesis and analysis of linear and nonlinear acoustical vortices," *Phys. Rev. E, Stat. Phys. Plasmas Fluids Relat. Interdiscip. Top.*, vol. 71, no. 6, p. 066616, 2005.
- [10] P. L. Marston, "Axial radiation force of a Bessel beam on a sphere and direction reversal of the force," *J. Acoust. Soc. Amer.*, vol. 120, no. 6, pp. 3518–3524, 2006.
- [11] F. G. Mitri, "Negative axial radiation force on a fluid and elastic spheres illuminated by a high-order Bessel beam of progressive waves," *J. Phys. A, Math. Theor.*, vol. 42, no. 24, p. 245202, 2009.
- [12] L. Zhang and P. L. Marston, "Axial radiation force exerted by general non-diffracting beams," *J. Acoust. Soc. Amer.*, vol. 131, no. 4, pp. EL329–EL335, 2012.
- [13] P. L. Marston, "Radiation force of a helicoidal Bessel beam on a sphere," *J. Acoust. Soc. Amer.*, vol. 125, no. 6, pp. 3539–3547, 2009.
- [14] D. Baresch, J. L. Thomas, and R. Marchiano, "Spherical vortex beams of high radial degree for enhanced single-beam tweezers," *J. Appl. Phys.*, vol. 113, no. 18, p. 184901, 2013.
- [15] F. C. Ngo, E. S. Ebbini, and C. A. Cain, "An experimental analysis of a sector-vortex phased array prototype," in *Proc. IEEE Ultrason. Symp.*, Oct. 1989, vol. 281, no. 86, pp. 999–1002.
- [16] G. T. Clement and K. Hynynen, "Micro-receiver guided transcranial beam steering," *IEEE Trans. Ultrason., Ferroelectr., Freq. Control*, vol. 49, no. 4, pp. 447–453, Apr. 2002.
- [17] H. Wang, E. S. Ebbini, M. O'Donnell, and C. A. Cain, "Phase aberration correction and motion compensation for ultrasonic hyperthermia phased arrays: Experimental results," *IEEE Trans. Ultrason., Ferroelectr., Freq. Control*, vol. 41, no. 1, pp. 34–43, Jan. 1994.
- [18] D. R. Daum, M. T. Buchanan, T. Fjeld, and K. Hynynen, "Design and evaluation of a feedback based phased array system for ultrasound surgery," *IEEE Trans. Ultrason., Ferroelectr., Freq. Control*, vol. 45, no. 2, pp. 431–438, Mar. 1998.
- [19] K. Hynynen and F. A. Jolesz, "Demonstration of potential noninvasive ultrasound brain therapy through an intact skull," *Ultrasound Med. Biol.*, vol. 24, no. 2, pp. 275–283, 1998.
- [20] G. T. Clement, J. Sun, T. Giesecke, and K. Hynynen, "A hemisphere array for non-invasive ultrasound brain therapy and surgery," *Phys. Med. Biol.*, vol. 45, no. 12, pp. 3707–3719, 2000.
- [21] K. Hynynen *et al.*, "500-element ultrasound phased array system for noninvasive focal surgery of the brain: A preliminary rabbit study with *ex vivo* human skulls," *Magn. Reson. Med.*, vol. 52, no. 1, pp. 100–107, 2004.
- [22] F. Wu, J. L. Thomas, and M. Fink, "Time reversal of ultrasonic fields. II. Experimental results," *IEEE Trans. Ultrason., Ferroelectr., Freq. Control*, vol. 39, no. 5, pp. 567–578, Sep. 1992.
- [23] M. Fink and C. Prada, "Acoustic time-reversal mirrors," *Inverse Problems*, vol. 17, no. 1, p. R1, 2001.
- [24] C. Prada, S. Manneville, D. Spoliensky, and M. Fink, "Decomposition of the time reversal operator: Detection and selective focusing on two scatterers," *J. Acoust. Soc. Amer.*, vol. 99, no. 4, pp. 2067–2076, 1996.
- [25] J. L. Thomas and M. A. Fink, "Ultrasonic beam focusing through tissue inhomogeneities with a time reversal mirror: Application to transskull therapy," *IEEE Trans. Ultrason., Ferroelectr., Freq. Control*, vol. 43, no. 6, pp. 1122–1129, Nov. 1996.
- [26] M. Pernot, J.-F. Aubry, M. Tanter, J.-L. Thomas, and M. Fink, "High power transcranial beam steering for ultrasonic brain therapy," *Phys. Med. Biol.*, vol. 48, no. 16, pp. 2577–2589, 2003.
- [27] E. S. Ebbini and C. A. Cain, "Multiple-focus ultrasound phased-array pattern synthesis: Optimal driving-signal distributions for hyperthermia," *IEEE Trans. Ultrason., Ferroelectr., Freq. Control*, vol. 36, no. 5, pp. 540–548, Sep. 1989.
- [28] M. Lu, M. Wan, F. Xu, X. Wang, and X. Chang, "Design and experiment of 256-element ultrasound phased array for noninvasive focused ultrasound surgery," *Ultrasonics*, vol. 44, no. 22, pp. 325–330, 2006.
- [29] M. Lu, M. Wan, F. Xu, X. Wang, and H. Zhong, "Focused beam control for ultrasound surgery with spherical-section phased array: Sound field calculation and genetic optimization algorithm," *IEEE Trans. Ultrason., Ferroelectr., Freq. Control*, vol. 52, no. 8, pp. 1270–1290, Aug. 2005.
- [30] G. T. Clement and K. Hynynen, "Field characterization of therapeutic ultrasound phased arrays through forward and backward planar projection," *J. Acoust. Soc. Amer.*, vol. 108, no. 1, pp. 441–446, 2000.
- [31] O. A. Sapozhnikov, S. A. Tsysar, V. A. Khokhlova, and W. Kreider, "Acoustic holography as a metrological tool for characterizing medical ultrasound sources and fields," *J. Acoust. Soc. Amer.*, vol. 138, no. 3, pp. 1515–1532, 2015.
- [32] V. A. Khokhlova *et al.*, "Design of HIFU transducers to generate specific nonlinear ultrasound fields," *Phys. Procedia*, vol. 87, pp. 132–138, Jan. 2016.
- [33] R. T. Hekkenberg, K. Beissner, B. Zeqiri, R. A. Bezemer, and M. Hodnett, "Validated ultrasonic power measurements up to 20 W," *Ultrasound Med. Biol.*, vol. 27, no. 3, pp. 427–438, 2001.
- [34] *Ultrasonics—Field Characterization—In Situ Exposure Estimation in Finite-Amplitude Ultrasonic Beams*, Standard IEC/TS61949:2007, 2007.
- [35] J. D. Maynard, E. G. Williams, and Y. Lee, "Nearfield acoustic holography: I. Theory of generalized holography and the development of NAH," *J. Acoust. Soc. Amer.*, vol. 78, no. 4, pp. 1395–1413, 1985.
- [36] P. A. Lewin, N. Barrie-Smith, M. Ide, K. Hynynen, and M. Macdonald, "Interlaboratory acoustic power measurement," *J. Ultrasound Med.*, vol. 22, no. 2, pp. 207–213, 2003.
- [37] B. Zeqiri and M. Hodnett, "Measurements, phantoms, and standardization," *Proc. Inst. Mech. Eng. H, J. Eng. Med.*, vol. 224, no. 2, pp. 375–391, 2010.
- [38] S. Maruvada, G. R. Harris, B. A. Herman, and R. L. King, "Acoustic power calibration of high-intensity focused ultrasound transducers using a radiation force technique," *J. Acoust. Soc. Amer.*, vol. 121, no. 3, pp. 1434–1439, 2007.
- [39] W. Shou *et al.*, "Acoustic power measurement of high intensity focused ultrasound in medicine based on radiation force," *Ultrasonics*, vol. 44, no. 22, pp. 17–20, 2006.
- [40] B. Delannoy, H. Lasota, C. Bruneel, R. Torguet, and E. Bridoux, "The infinite planar baffles problem in acoustic radiation and its experimental verification," *J. Appl. Phys.*, vol. 50, no. 8, pp. 5189–5195, 1979.
- [41] I. Freund, "Critical point explosions in two-dimensional wave fields," *Opt. Commun.*, vol. 159, no. 1, pp. 99–117, 1999.
- [42] M. R. Dennis and J. B. Götte, "Instability of higher-order optical vortices analyzed with a multi-pinhole interferometer," *Phys. Rev. Lett.*, vol. 109, no. 18, pp. 1018–1020, 2012.
- [43] A. Kumar, P. Vaity, J. Bhatt, and R. P. Singh, "Stability of higher order optical vortices produced by spatial light modulators," *J. Mod. Opt.*, vol. 60, no. 20, pp. 1696–1700, 2013.
- [44] *Ultrasonics—Field Characterization—Specification and Measurement of Field Parameters for High Intensity Therapeutic Ultrasound (HITU) Transducers and Systems.*, Standard IEC TS 62556:2014, 2014.



**Mohamed A. Ghanem** received the B.S. degree in civil engineering and the M.S. degree in aeronautics and astronautics engineering from the University of Washington, Seattle, WA, USA, in 2009 and 2012, respectively, where he is currently pursuing the Ph.D. degree with the Department of Aeronautics and Astronautics Engineering.

He was a Structural Engineer with SIE, Mukilteo, WA, USA, from 2012 to 2014. Most of his research focused on linear and nonlinear finite-element analysis under mechanical and thermal loads for metallic and composite components. His research interests include the development of 3-D acoustical traps for macroscopic objects and development of advanced holographic lenses, stress wave propagation, optimization techniques, and finite-element modeling.

Mr. Ghanem received the Engineer-in-Training Certificate from the State of Washington, Seattle, WA, USA, in 2009.



**Adam D. Maxwell** received the B.S. degree in electrical engineering from the University of Washington, Seattle, WA, USA, in 2006, the M.S. degree in electrical engineering and the Ph.D. degree in biomedical engineering from the University of Michigan, Ann Arbor, MI, USA, in 2007 and 2012, respectively.

From 2012 to 2014, he was a Post-Doctoral Fellow with the Department of Urology, University of Washington, where he is currently an Acting Assistant Professor. His research interests include

the development of image-guided ultrasound therapies including focused ultrasound for mechanical tissue ablation (histotripsy) and lithotripsy.



**Wayne Kreider** received the B.S. and M.S. degrees in engineering mechanics from Virginia Tech, Blacksburg, VA, USA, in 1993 and 1995, respectively, and the Ph.D. degree in bioengineering from the University of Washington, Seattle, WA, USA, in 2008.

He was an Engineer with the Naval Surface Warfare Center, Dahlgren, VA, USA, from 1996 to 1997. He was with Dominion Engineering Inc., Reston, VA, USA, from 1997 to 2001. In 2000, he became a Licensed Professional Engineer in the

Commonwealth of Virginia. Much of his research during this time focused on the development and qualification of ultrasonic cleaning technologies for steam generators and fuel in nuclear power plants. Since 2001, he has worked at the Center for Industrial and Medical Ultrasound in the Applied Physics Laboratory (APL) at the University of Washington in Seattle as a student (Ph.D., 2008, bioengineering), a Research Associate, and a Senior Engineer (since 2012). His research interests include acoustic cavitation, transport processes in oscillating bubbles, therapeutic ultrasound, and ultrasound metrology.

Dr. Kreider is a member of the Acoustical Society of America. He has been a technical representative for the Committee on Standards since 2013. Related to the characterization of intense ultrasound fields, he is a U.S. delegate to the International Electrotechnical Commission as a member of Technical Committee 87, Working Group 6, since 2015.



**Bryan W. Cunitz** received the B.A. degree in physics from Colby College, Waterville, ME, USA, in 1999, the B.S. degree in electrical engineering from Dartmouth College, Hanover, NH, USA, in 2000, and the M.S. degree in electrical engineering from the University of Washington, Seattle, WA, USA, in 2005.

He is a Senior Research Engineer with the University of Washington, Seattle, WA, USA, where he is involved in improving ultrasound systems for the detection of kidney stones, therapeutic applications

of focused ultrasound for the breaking and repositioning of kidney stones, image-guided acoustic hemostasis, transducer development, and acoustic output measurements.



**Vera A. Khokhlova** received the M.S. degree in physics from Moscow State University (MSU), Moscow, Russia, in 1986, and the Ph.D. and D.Sc. degrees in acoustics from MSU, in 1991 and 2012, respectively.

She is currently an Associate Professor with the Department of Acoustics, Physics Faculty, Moscow State University. Since 1995, she has been with the Center for Industrial and Medical Ultrasound, Applied Physics Laboratory, University of Washington, Seattle, WA, USA. Her research interests

include field of nonlinear acoustics, therapeutic ultrasound including metrology and bioeffects of high intensity focused ultrasound fields, shock wave focusing, nonlinear wave propagation in inhomogeneous media, and nonlinear modeling.

Dr. Khokhlova has been a fellow since 2008 and has served as a member for the Executive Council of the Acoustical Society of America from 2012 to 2015, a member for the Board of the International Society for Therapeutic Ultrasound from 2004 to 2008 and from 2011 to 2014, and a member of the "Physical Ultrasound" Division of the Scientific Council on Acoustics of the Russian Academy of Sciences since 2009. She has been an Associate Editor of the IEEE TRANSACTIONS ON ULTRASONICS, FERROELECTRICS, AND FREQUENCY CONTROL since 2013.



**Oleg A. Sapozhnikov** received the M.S. degree in physics, and the Ph.D. and D.Sc. degrees in acoustics from Moscow State University (MSU), Moscow, Russia, in 1985, 1988, and 2008, respectively.

He is currently a Professor with the Department of Acoustics, Physics Faculty, MSU. Since 1996, he has been with the Applied Physics Laboratory, Center for Industrial and Medical Ultrasound, University of Washington, Seattle, WA, USA. His research interests include fields of physical acoustics, nonlinear wave phenomena, medical ultrasound including shock wave lithotripsy, high intensity focused ultrasound, and ultrasound-based imaging.

Dr. Sapozhnikov has been a member of the International Society for Therapeutic Ultrasound since 2001, a member of the Board of the International Congress on Ultrasonics since 2008, and the Head of the "Physical Ultrasound" Division of the Scientific Council on Acoustics of the Russian Academy of Sciences since 2009. He has been a fellow of the Acoustical Society of America since 2009. He was a recipient of the M.V. Lomonosov Prize in Physics (1991), the Prize of the European Academy for Young Russian Scientists (1994), and the Early Career Award of the International Commission for Acoustics (2004).



**Michael R. Bailey** received the B.S. degree in mechanical engineering from Yale University, New Haven, CT, USA, in 1991, and the M.S. and Ph.D. degrees in mechanical engineering from the University of Texas at Austin, Austin, TX, USA, in 1994 and 1997, respectively.

He is currently a Senior Principal Engineer with the Applied Research Laboratory, an Associate Professor of mechanical engineering, and Adjunct Associate Professor of urology, University of Washington, Seattle, WA, USA. He is currently focused on developing ultrasound-based technology to reposition kidney stones. His research

interests include cavitation, shock wave lithotripsy, high intensity focused ultrasound, and ultrasound imaging.

Dr. Bailey is a fellow of the Acoustical Society of America (ASA) and served on the ASA Executive Council. He received early career awards from ASA in 2004 and ISTU in 2008. He served on the Board of the International Society for Therapeutic Ultrasound from 2009 to 2012, the Bioeffects Committee of the American Institute for Ultrasound in Medicine from 2006 to 2012, and the Biomedical Acoustics Technical Committee of the ASA from 2005 to 2008.